Microglia promote infiltration and polarization of macrophages in cerebral ischemia-reperfusion via the reactive oxygen species-SPI1-CCL9 axis

XIANFENG KUANG[1,2*], ZHANGXIANG PENG[3*], YAO YANG[4*], SHAOQUAN PU[1,2], MOU ZHANG[2,5], JIAYUE WANG[6], JUN TAO[7], SHIXIANG LI[8] and DONG ZHAN[2]

[1]Department of Orthopaedics, 920th Hospital of Joint Logistics Support Force, Kunming Medical University, Kunming, Yunnan 650032, P.R. China; [2]School of Basic Medical Sciences, Kunming Medical University, Kunming, Yunnan 650500, P.R. China; [3]Department of Geriatrics III, Jiujiang Fifth People's Hospital, Jiujiang, Jiangxi 332000, P.R. China; [4]Department of Intensive Care Medicine, Jiangxi Fengcheng Hospital of Traditional Chinese Medicine, Yichun, Jiangxi 331100, P.R. China; [5]Department of Neurology, Sanming First Hospital Affiliated to Fujian Medical University, Sanming, Fujian 365000, P.R. China; [6]The First Clinical Medical College, Yunnan University of Chinese Medicine, Kunming, Yunnan 650500, P.R. China; [7]Yunnan Key Laboratory of Stem Cell and Regenerative Medicine, School of Rehabilitation, Kunming Medical University, Kunming, Yunan 650500, P.R.China; [8]School of Pharmaceutical Sciences, Kunming Medical University, Kunming, Yunan 650500, P.R. China

Received December 15, 2025; Accepted October 9, 2026

DOI: 10.3892/mmr.2026.14064

Abstract. The aim of the present study was to investigate the role of microglia in promoting macrophage infiltration and polarization during cerebral ischemia-reperfusion (I/R) injury through the reactive oxygen species (ROS)-Spi-1 proto-oncogene (SPI1)-chemokine (C-C motif) ligand 9 (CCL9) signalling axis. Using a cerebral I/R *in vitro* and *in vivo* model, microglial activation and macrophage dynamics were assessed. ROS levels were quantified, and SPI1 expression in microglia was analysed. CCL9 secretion was measured, and its impact on macrophage migration and polarization was evaluated *in vitro*. CCL9 antibody and RNA interference approaches were used to interrogate the signalling pathway. Following cerebral I/R, microglial activation led to increased ROS production, and increased SPI1 and CCL9 expression. This, in turn, increased CCL9 secretion, which attracted macrophages to the site of ischemia and promoted their polarization towards a pro-inflammatory phenotype. Inhibition of the ROS-SPI1-CCL9 axis significantly reduced macrophage infiltration and altered their polarization state. The results of the present study demonstrated that microglia facilitated macrophage infiltration and polarization in cerebral I/R via the ROS-SPI1-CCL9 axis, highlighting a potential therapeutic target for mitigating neuroinflammatory damage after a cerebral ischemic stroke.

Correspondence to: Mr. Dong Zhan, School of Basic Medical Sciences, Kunming Medical University, 1168 West Chunrong Road, Yuhua Avenue, Chenggong, Kunming, Yunnan 650500, P.R. China
E-mail: zhan.dong@outlook.com

*Contributed equally

Key words: cerebral ischemic stroke, ischemia-reperfusion, microglial, macrophage, C-C motif chemokine ligand 9

Introduction

Cerebral ischaemic stroke, a leading cause of morbidity and mortality worldwide, is characterised by disruption of blood flow to the brain, resulting in neuronal death and neurological deficits (1). The pathophysiology of cerebral ischaemic stroke is multifaceted, involving excitotoxicity, oxidative stress, inflammation, and multiple forms of programmed cell death, including apoptosis, ferroptosis, pyroptosis and necroptosis (2). Restoration of blood flow is a critical therapeutic objective for salvaging ischaemic brain tissue. However, reperfusion itself may exacerbate brain injury, a phenomenon known as ischaemia-reperfusion injury (IRI) (3). This paradoxical effect results from a cascade of pathophysiological events, including oxidative stress, leukocyte infiltration, platelet aggregation, complement activation, mitochondrial dysfunction and blood-brain barrier (BBB) disruption, collectively contributing to cerebral oedema, haemorrhagic transformation and neuronal death (4,5). Despite advances in reperfusion therapies, such as thrombolysis with tissue plasminogen activator and mechanical thrombectomy, the deleterious effects of IRI remain a major challenge in stroke management (6).

Both resident microglia and infiltrating monocytes are key mediators of the inflammatory response. Their dual roles in promoting tissue damage and facilitating repair underscore their importance in the pathophysiology of cerebral ischemia-reperfusion (I/R) injury (7). During the acute phase of cerebral I/R injury, macrophages are rapidly activated and contribute to the release of pro-inflammatory cytokines,

including TNF-α and IL-1β, which exacerbate neuronal damage and disrupt the BBB (2,7,8). Macrophage activation further amplifies neuroinflammation through the release of IL-18 and IL-1β, leading to pyroptosis (8). This inflammatory cascade is further aggravated by neutrophil recruitment and the generation of reactive oxygen species (ROS), which perpetuate oxidative stress and cellular damage (8). However, macrophages may also adopt a reparative phenotype, particularly during the subacute and chronic phases of I/R injury (9). Studies have demonstrated that CD68-expressing macrophages, classified as M1 macrophages and abundant within infarcted brain regions, are important sources of TGF-β, a cytokine that promotes angiogenesis, neurogenesis and scar formation (10,11). Microglial activation during I/R is closely associated with the production of inflammatory cytokines, including IL-1β and TNF-α, as well as matrix metalloproteinases, which contribute to BBB disruption and neuronal apoptosis (12).

However, the interplay between microglia and macrophages remains unclear. It is uncertain whether microglia recruit monocytes or macrophages to ischaemic and reperfused brain tissue through the release of chemokines, thereby contributing to the inflammatory response. In the present study, cerebral I/R hub genes were identified from public databases using bioinformatic approaches. Integrated machine-learning (ML) algorithms and transcription factor (TF) prediction analyses were applied to identify target genes. Subsequently, cerebral I/R models were used to validate the target genes and investigate their functions *in vivo* and *in vitro*. These findings may improve understanding of the relationship between microglia and infiltrating macrophages and provide further insight into the mechanisms underlying cerebral I/R injury.

Materials and methods

Data collection. RNA sequencing datasets were obtained from the Gene Expression Omnibus (GEO) database. The GSE137482 dataset was used for hub-gene screening and comprised 12 sham samples and 12 middle cerebral artery occlusion (MCAO) samples (13). In addition, the single-cell RNA sequencing dataset GSE174574 included nine sham samples and nine MCAO samples (14).

Differentially expressed gene (DEG) analysis. Data normalisation and differential expression analyses were performed using R software (version 4.2.0; https://www.r-project.org) and the *limma* package Differential expression analysis of GSE137482 was conducted using the *DESeq2* package to identify DEGs between the MCAO and control groups. Genes with an adjusted $P<0.05$ and $|\log_2$ fold change (FC)$|>1.0$ were considered differentially expressed. Weighted gene co-expression network analysis (WGCNA) was performed to identify gene modules associated with cerebral infarction. Gene Significance and Module Membership thresholds of >0.20 and >0.80, respectively, were used for module selection.

Single-cell RNA sequencing analysis. The GSE174574 dataset was processed using the Seurat package (15). Cells were initially filtered according to the following criteria: Cell count between 3 and 50, nFeature_RNA >50, and mitochondrial gene percentage <5%. Quality-control thresholds were further refined using median absolute deviation (MAD)-based automatic filtering. The quality control (QC) covariates log1p_total_counts, log1p_n_genes_by_counts, and pct_counts_in_top_20_genes were filtered using a threshold of five times the MAD for each variable.

Cells were clustered using the 'FindClusters' function with a resolution of 0.6, yielding 20 cell populations. Microglial marker genes were identified using the Wilcoxon rank-sum test implemented in Scanpy (16). Cell-type annotation was performed using reference markers obtained from the scType database (https://sctype.app). Cell-cell communication analyses were conducted using the CellChat database (https://github.com/jinworks/CellChat). Microglial subtypes were identified using specific markers from the CellMarker database (http://117.50.127.228/CellMarker/).

DEGs in microglial populations were identified using a pseudobulk approach. Gene expression counts from microglial subsets were aggregated within each sample to generate a pseudobulk expression matrix that approximated conventional bulk RNA sequencing data. Differential expression analysis was subsequently performed using the *DESeq2* package (17). Genes with $|\log_2 FC|>1$ and an adjusted $P<0.05$ were retained for further analysis.

Functional exploration of hub genes. Gene annotation was performed using the *org.Hs.eg.db* package and the KEGG REST API. Functional enrichment analyses were conducted using the *clusterProfiler* package. Gene sets containing between 5-5,000 genes were included, and $P<0.05$ was considered statistically significant.

A protein-protein interaction (PPI) network was constructed using the STRING database (https://string-db.org) with a minimum confidence score of 0.4 and visualised in Cytoscape (version 3.9.1; https://cytoscape.org). Network topology analysis was performed using the CytoNCA plugin to calculate node degree values. Hub-gene identification was further conducted using the CytoHubba plugin with the MNC, Degree, EPC, Bottleneck, Closeness, Radiality and Betweenness algorithms.

Diagnostic biomarker screening based on ML. Diagnostic biomarkers were identified using two ML approaches: Random forest (RF) analysis and least absolute shrinkage and selection operator (LASSO) logistic regression, implemented using the *randomForest* and *glmnet* packages, respectively (18,19).

For LASSO logistic regression, coefficient trajectory plots were generated to illustrate coefficient shrinkage under different penalty parameters. The optimal regularisation parameter (λ) was determined using binomial deviance analysis. For RF analysis, variable importance was evaluated using the mean decrease in the Gini coefficient. Genes identified by both ML approaches were selected as candidate hub genes for subsequent investigation.

TF prediction. Using the JASPAR (https://jaspar.elixir.no/) and TRRUST databases (https://www.grnpedia.org/trrust/), TFs associated with all hub genes were predicted and analysed. The TF intersection from both databases was imported into Cytoscape to visualize interactions between TFs and

Table I. siRNA sequences to silence SPI1 gene expression.

Gene name	RNA Oligo Sequence (5'-3')
Homo sapiens (NM_003120.3)	Sense: UAACUUUACUUGUUUUUUGGG Antisense: CAAAAAACAAGUAAAGUUAUU
Mus musculus (NM_011355.2)	Sense: AUUUUACUUGUCUUUAGUGAC Antisense: CACUAAAGACAAGUAAAAUUA
Negative control (siNC)	Sense: UUCUCCGAACGUGUCACGUUU Antisense: ACGUGACACGUUCGGAGAAUU

siRNA/si, small interfering RNA; SPI1, Spi-1 proto-oncogene.

hub genes. Their relationships were identified using FIMO to detect binding sites with q-value<0.05 after FDR adjustment.

Cell culture and transfection. BV2 cells (National Collection of Authenticated Cell Culture) were cultured in high-glucose DMEM supplemented with 10% FBS and 100 U/ml penicillin-streptomycin. Cells were maintained at 37˚C in a humidified atmosphere containing 5% CO_2 and passaged every 3 days. For experiments, cells were seeded at $1x10^5$ cells/ml in 6-well plates and cultured until they reached 85% confluency. BV2 cells were transfected with either Spi-1 proto-oncogene (SPI1) small interfering RNA (siRNA; Shanghai GenePharma Co., Ltd.) or negative control siRNA using Lipofectamine RNAiMAX Reagent (Invitrogen; Thermo Fisher Scientific, Inc.) according to the manufacturer's instructions. The siRNA duplexes were diluted in Opti-MEM I Reduced Serum Medium, and Lipofectamine RNAiMAX was separately diluted in the same medium. Both were combined to form transfection complexes and incubated at room temperature (RT) for 20 min. The complexes with 10 nM siRNA were then added to cells cultured in antibiotic-free DMEM at 37˚C in a humidified 5% CO_2 incubator for 48 h before subsequent assays. The siRNA sequences are listed in Table I.

An oxygen-glucose deprivation/reperfusion (OGD/R) procedure was used to mimic IRI *in vitro*. During the deprivation phase, the culture medium was replaced with glucose-free DMEM pre-equilibrated in a hypoxic chamber (1% O_2, 5% CO_2) for 2 h. Subsequently, during the reperfusion phase, high-glucose DMEM was restored, and the cells were returned to normoxic conditions (21% O_2, 5% CO_2) for 12 h. In total, four experimental groups were established, comprising BV2 cells treated with either SPI1 siRNA or negative control siRNA under OGD/R conditions (n=5).

Male C57BL/6 mice (8-10 weeks old, 22-25 g) were purchased from the Animal Experiment Center of Kunming Medical University (approval no. KMMU20240416; Kunming, China). Mice were euthanised by an overdose of sodium pentobarbital (150 mg/kg) administered via intraperitoneal injection. Death was confirmed by cessation of heartbeat and respiration, followed by cervical dislocation. Bilateral femurs were harvested and flushed with ice-cold PBS using a 27G needle (n=5). Cells were filtered through a 70-μm cell strainer, centrifuged at 400 x g for 5 min, and red blood cells were lysed using ammonium chloride-potassium buffer. The cells were then resuspended in DMEM supplemented with 10% FBS and 20 ng/ml recombinant mouse M-CSF. The resulting cell suspension was seeded into T25 flasks and cultured at 37˚C in 5% CO_2. The medium was replaced every 2 days. After 7 days, mouse bone marrow-derived macrophages (BMDMs) had matured and adhered to the culture surface for subsequent use. Macrophage identity was confirmed by flow cytometry based on $CD11b^+$ and $F4/80^+$ expression.

A Transwell system was established with BMDMs ($5x10^4$ cells/well) seeded in the lower chamber and BV2 cells ($2x10^4$ cells/insert), treated with or without SPI1 siRNA, seeded in the upper chamber of a 24-well plate. The media in all chambers was replaced with culture medium without FBS and incubated at 37˚C in 5% CO_2 for 24 h prior to further analysis.

Chromatin immunoprecipitation-quantitative PCR (ChIP-qPCR) for SPI1 binding to the chemokine (C-C motif) ligand 9 (CCL9) promoter. ChIP-qPCR was performed to assess SPI1 binding to the CCL9 promoter. BV2 cells were cultured to 70-80% confluency. For cross-linking, cells were treated with 1% formaldehyde in serum-free medium for 10 min at RT, followed by quenching with 0.125 M glycine. Cells were washed twice with ice-cold PBS, harvested by scraping, and pelleted by centrifugation with 500 x g for 5 min at 4˚C. Nuclear lysates were prepared by resuspending cell pellets in lysis buffer containing 1% SDS, 10 mM EDTA, and 50 mM Tris-HCl (pH 8.1), supplemented with protease inhibitors. Chromatin was sheared into fragments of 200-500 bp by sonication (30 cycles of 30 sec on and 30 sec off at high intensity using a Bioruptor). Cellular debris was removed by centrifugation at 20,000 x g for 10 min at 4˚C.

For immunoprecipitation, 50 μg sheared chromatin was diluted in dilution buffer containing 0.01% SDS, 1.1% Triton X-100, 1.2 mM EDTA, 16.7 mM Tris-HCl (pH 8.1), and 167 mM NaCl, and incubated overnight at 4˚C with 2-5 μg anti-SPI1 antibody or rabbit IgG as a negative control (Santa Cruz Biotechnology, Inc.; cat. no. sc-352, validated for ChIP). DNA-protein complexes were captured using 30 μl protein A/G magnetic beads for 2 h at 4˚C and washed sequentially with low-salt, high-salt, LiCl, and TE buffers. Chromatin was eluted at 65˚C for 30 min using elution buffer containing 1% SDS and 0.1 M $NaHCO_3$. Cross-links were reversed overnight at 65˚C, followed by DNA purification using a QIAquick PCR Purification Kit (cat. no. 28106; Qiagen, Inc.) according to the manufacturer's protocol.

PCR was performed to determine CCL9 promoter enrichment using primers targeting the SPI1 consensus-binding motif. Input DNA (2%) was used for normalization. Enrichment was calculated as percentage input using the $2^{-\Delta\Delta Cq}$ method and compared with IgG controls (20).

Transmigration assay. For the *in vitro* assessment of the invasive capacity of primary cultured microglial cells, Transwell chambers equipped with 8.0 μm PET membranes (BioCoat Matrigel Invasion Chambers; Corning, Inc.) were used. BMDMs were suspended in DMEM supplemented with 0.5% BSA (cat. no. 9048-46-8; Sangon Biotech, Co., Ltd.) and seeded into the upper chambers at a density of $5x10^4$ cells per insert. BV2 cells, either untreated or treated with siRNA, were seeded into the lower chambers of 24-well plates. Following 24 h of incubation, non-invading cells remaining on the upper surface of the membrane were removed mechanically. Cells that had migrated to the lower surface of the membrane were fixed with 4% paraformaldehyde for 10 min at RT. After twice washed with demineralized water for 2 min and stained with 0.1% crystal violet for 10 min at RT. The invasive BMDMs were visualised under a light microscope at x20 magnification and quantified by counting the number of stained cells.

Mice cerebral I/R model. Male C57BL/6 mice (8-10 weeks old, 22-25 g) were purchased from the Animal Experiment Centre of Kunming Medical University (approval no. KMMU20240416). Mice were housed under standard conditions with *ad libitum* access to food and water. Their facility was maintained at 20-26˚C with 40-70% relative humidity and a 12-h light/12-h dark cycle. Animals were randomly assigned to the sham, MCAO + IgG, and MCAO + anti-CCL9 groups (n=6 per group). Mice were anaesthetised with 3-4% isoflurane and maintained at 1.5-2% via a nose cone. Core body temperature was monitored using a rectal probe and maintained at 37˚C using a heating pad. A midline neck incision was made to expose the right common carotid artery, external carotid artery (ECA), and internal carotid artery (ICA). The ECA was ligated distally, and a 6-0 nylon monofilament (silicone-coated; diameter, 0.21-0.23 mm) was inserted through the ECA stump into the ICA until resistance was felt (9-10 mm from the bifurcation). Occlusion was confirmed by laser Doppler flowmetry (PeriFlux System 5000, PERIMED), which showed a ≥80% reduction in cerebral blood flow (CBF). After 60 min of occlusion, the filament was withdrawn to restore CBF.

Mice in the MCAO + IgG and MCAO + anti-CCL9 groups separately received intravenous injections via the tail vein of 200 μl PBS containing either 200 μg isotype IgG (cat. no. K011730RR; Wuhan Servicebio Technology Co., Ltd.) or 200 μg anti-CCL9 antibody (cat. no. K009557P; Wuhan Servicebio Technology Co., Ltd.) on postoperative days 1 and 6 (n=6 per group). Mice in the sham group underwent the same surgical procedure without filament insertion and received 200 μl PBS intravenously. The sham and MCAO + IgG groups served as controls for evaluating the specific neuroprotective effects of CCL9 blockade.

At 72 h after the final intervention, all mice were euthanised by isoflurane overdose using a precision vaporiser and a dedicated anaesthesia induction chamber supplied with 5% isoflurane in oxygen. Following respiratory arrest, administration of high-concentration isoflurane was maintained for at least an additional 2 min to ensure irreversible death. Death was confirmed by the absence of respiration and heartbeat, together with pupillary dilatation. Following thoracotomy, the circulatory system was transcardially perfused with ice-cold PBS. Brains were then collected for 2,3,5-triphenyltetrazolium chloride (TTC) staining. Animals with an infarct area comprising at least 15% of the ipsilateral cerebral hemisphere were considered successful MCAO models. Mice that did not meet this TTC-based criterion or died before the scheduled staining time point were excluded. In the present study, six mice were initially assigned to each group; however, one mouse was excluded due to unsuccessful MCAO modelling. Consequently, five mice from each group were included in the subsequent RNA and protein analyses.

Rotarod test for mouse locomotor function. The XR-6C/6D rotarod apparatus (Xingruan) consists of an acrylic box divided into six compartments with a rotating shaft. Before cerebral I/R surgery, each mouse underwent training on the rotarod apparatus (30 mm diameter, 15 rpm) for up to 300 sec. Following the surgical procedure, mice were assessed on day 7 after injury. The duration for which an animal remained on the rotating rod was used as an indicator of balance, coordination, physical condition, and motor function. The cut-off time was set at 300 sec, as described previously (21).

TTC staining of mouse brain tissue. The intact brains were frozen at -20˚C for 20 min to facilitate sectioning. Coronal brain sections (2 mm thick) were prepared using a brain matrix. The sections were rinsed with PBS to remove residual blood, then immersed in a 2% TTC solution (0.1 M PBS, pH 7.4) at 37˚C for 30 min in the dark. Normal tissue stained red because of NADH-dependent dehydrogenase activity, whereas infarcted tissue remained white. After staining, the sections were transferred to 4% paraformaldehyde and fixed for 24 h at RT. Images of the sections were captured using a digital camera with a scale ruler in the frame. Infarct volume were quantified using ImageJ software (version 1.54p, National Institutes of Health). Relative infarcted volume percentage was calculated with following formula: (contralateral hemisphere volume - ipsilateral non-infarcted hemisphere volume)/contralateral hemisphere volume x100% (22).

Flow cytometric analysis of macrophage surface markers. Cultured BMDMs were harvested with 0.25% trypsin for 5 min and adjusted to $1.0x10^7$ cells/ml in DMEM supplemented with 10% FBS. A 100 μl aliquot of the cell suspension was transferred into 1,000 μl PBS containing 10% FBS and centrifuged at 900 x g for 3 min. The cell pellets were resuspended in 100 μl PBS/10% FBS. Subsequently, 5 μl each of FITC-conjugated anti-CD206, PE-conjugated anti-CD68, APC-conjugated anti-CD11b, and FITC-conjugated anti-F4/80 antibodies (Abcam) were added. After brief vortexing, the cells were incubated at RT in the dark for 30 min. Following incubation, 1,000 μl PBS/10% FBS was added, and the cells were centrifuged at 900 x g for 3 min. The cell pellets were resuspended in 500 μl PBS/10% FBS and fixed with 500 μl PBS containing 4% paraformaldehyde at RT in the dark for

15 min. Cells were then centrifuged again and finally resuspended in 1,000 μl PBS/10% FBS. Flow cytometric analysis was performed using a BD FACSCanto II flow cytometer (BD Biosciences), and data were analysed with BD FACSDiva software (version 8.0, BD Biosciences).

Flow cytometric detection of intracellular ROS. BV2 cells treated with or without SPI1 siRNA were seeded into 6-well plates ($1x10^5$ cells/well) and allowed to adhere overnight. Following OGD/R treatment, the culture medium was replaced with 1 ml serum-free DMEM containing 10 μM DCFH-DA (MilliporeSigma) per well. Cells were incubated at 37˚C for 30 min in the dark. After incubation, cells were washed twice with ice-cold PBS (pH 7.4) to remove excess extracellular probe. Cells were detached using 0.25% trypsin-EDTA and neutralised with complete culture medium. The cell suspensions were centrifuged at 900 x g for 3 min, resuspended in 500 μl PBS, and immediately analysed using a BD FACSCanto II flow cytometer.

Reverse transcription (RT)-qPCR. Total RNA was extracted from cells using TRIzol reagent (cat. no. B610409; Sangon Biotech, Co., Ltd.) and analysed by RT-qPCR. Green One-Step RT-qPCR SuperMix (TransGen Biotech Co., Ltd.) was used to determine the relative mRNA expression levels of CCL9 and SPI1 on an ABI StepOnePlus Real-Time PCR System (Applied Biosystems; Thermo Fisher Scientific, Inc.). Each 50 μl reaction contained 25 μl 2X FastKing RT-qPCR Buffer (SYBR Green), 2 μl 25X RT-PCR Enzyme Mix, 1.25 μl each of the forward and reverse primers (final concentration, 0.25 μM), 2 μl total RNA template, 5 μl ROX Reference Dye, and 14.75 μl RNase-free ddH_2O. Reverse transcription was performed at 50˚C for 30 min, followed by an initial denaturation step at 95˚C for 3 min. Amplification was performed with 40 cycles of denaturation at 95˚C for 15 sec and annealing/extension at 60˚C for 30 sec, during which fluorescence signals were acquired. Primer sequences are listed in Table II. Relative gene expression levels were normalised to β-actin and calculated using the $2^{-\Delta\Delta Cq}$ method. All reactions were performed five times to ensure reproducibility.

Western blotting. Fresh mouse cerebral tissue (20 mg per mouse) was washed three times with ice-cold PBS and homogenised in 200 μl RIPA lysis buffer (cat. no. C500005; Sangon Biotech, Co., Ltd.) supplemented with protease inhibitors. Tissue samples were homogenised using an automated tissue grinder (SWE-FP PLUS; Wuhan Servicebio Technology Co., Ltd.) for five cycles (10 sec per cycle) at 4˚C. Treated cells were lysed in 100 μl RIPA lysis buffer containing protease inhibitors and incubated on ice for 30 min. The lysates were centrifuged at 16,000 x g for 15 min at 4˚C, and the supernatants were collected for protein quantification using a BCA Protein Assay Kit (cat. no. ZJ101; Boulogne-Billancourt).

Equal quantities of protein (30 μg per lane) were separated by 10% SDS-PAGE and transferred onto PVDF membranes. Membranes were blocked with 5% skimmed milk in TBS-Tween-20 containing 0.1% Tween-20 (TBST; cat. no. C520009; Sangon Biotech, Co., Ltd.) for 2 h at 4˚C, sequentially incubated overnight at 4˚C with primary antibodies (1:5,000) against CCL9 (cat. no. 500-P117-50UG; Invitrogen; Thermo Fisher Scientific, Inc.), SPI1 (cat. no. ab230336; Abcam) and β-actin (cat. no. ab8227; Abcam) in the Antibody Dilution Buffer (cat. no. PS119, Shanghai Epizyme Biomedical Technology Co., Ltd). After washing, membranes were incubated with HRP-conjugated secondary antibodies (1:10,000) in the Antibody Dilution Buffer for 2 h at RT. Following three washes with TBST, protein bands were visualised using an enhanced chemiluminescence detection kit (cat. no. C510045-0100, Boulogne-Billancourt). Images and band intensities were acquired and quantified using an iBright FL1500 Imaging System (Invitrogen; Thermo Fisher Scientific, Inc.). β-actin served as the internal loading control for relative protein expression analysis.

Table II. Forward and reverse primers sequences for gene expression.

Gene name	Primer sequence (5'-3')
CCL9	F: CCCTCTCCTTCCTCATTCTTACA
	R: AGTCTTGAAAGCCCATGTGAAA
SPI1	F: AGGAGTCTTCTACGACCTGGA
	R: GAAGGCTTCATAGGGAGCGAT
iNOS	F: GTTCTCAGCCCAACAATACAAGA
	R: GTGGACGGGTCGATGTCAC
CCL9 promoter	F: ATTTCCAGTGAAATCATAG
	R: CTTTGTTTTGAATACTTAGTAC
IL1-β	F: GAAATGCCACCTTTTGACAGTG
	R: TGGATGCTCTCATCAGGACAG
TNF-α	F: CAGGCGGTGCCTATGTCTC
	R: CGATCACCCCGAAGTTCAGTAG
β-actin	F: GTGACGTTGACATCCGTAAAGA
	R: GCCGGACTCATCGTACTCC

F, forward; R, reverse; iNOS, inducible nitric oxide synthase; CCL9, chemokine (C-C motif) ligand 9; SPI1, Spi-1 proto-oncogene.

ELISA. The concentrations of IL-1β, IL-6, and TNF-α were determined using ELISA kits (cat. nos. MM-0040M2, MM-0163M2 and MM-0132M2; Jiangsu Meimian Industrial Co., Ltd.) according to the manufacturer's instructions. Protein samples were thawed at RT, and standards, biotinylated antibodies, Streptavidin-HRP diluent and TMB substrate were prepared before use. 96-well plates were pre-coated with capture antibody by these kits' supplier. Diluted samples or standards (100 μl/well) were added and incubated for 2 h at RT. Then, 50 μl biotinylated detective antibody was added and incubated for 1 h at RT. After the liquid was aspirated from each well and washed five times, 100 μl diluted Streptavidin-HRP solution was added and incubated for 1 h at RT. After a further five washes, 100 μl TMB substrate was added, and the plates were incubated in the dark for 30 min. The reaction was terminated by the addition of 100 μl 2 M H_2SO_4 Stop Reagent, and absorbance on 450 nm spectrophotometer was measured using a microplate reader (Varioskan LUX; Thermo Fisher Scientific, Inc.).

Statistical analysis. Statistical analyses were performed using R software (version 4.2.0) and GraphPad Prism 9.0 (Dotmatics). Quantitative data are presented as the mean ± standard error (SE). Data normality was assessed using the Shapiro-Wilk test. Differences between two groups with non-normally distributed quantitative data were analysed using the Mann-Whitney U test. Differences between two independent groups with normally distributed quantitative data were analysed using an unpaired Student's t-test. More than two groups' differences were analysed by Kruskal-Wallis test and multiple group differences were determined with Dunn's multiple comparisons post hoc test. $P<0.05$ was considered to indicate a statistically significant difference.

Results

Screening of hub genes using bioinformatics. DEGs identified from the transcriptomic dataset were visualized using a volcano plot (Fig. 1A). Compared with normal brain tissue, 2,424 genes were upregulated at least two-fold in MCAO brain tissue, whereas 148 genes were downregulated at least two-fold. As shown in Fig. 1B, WGCNA was performed to distinguish the control and MCAO phenotypes and to identify gene modules associated with MCAO. The hierarchical clustering dendrogram generated by WGCNA illustrated gene co-expression relationships based on topological overlap dissimilarity (left panel, Fig. 1B). Dynamic tree cutting initially identified multiple gene modules, represented by different colour bands, which were subsequently merged into eight modules based on eigengene similarity (lower panel). The heatmap shown in the right panel of (Fig. 1B) illustrates the correlations between the merged modules and the MCAO phenotype. Among these modules, the MEblue module demonstrated the strongest positive correlation with MCAO ($r=0.91$, $P=7.0\times10^{-10}$) and contained 2,325 genes.

Following quality control of the single-cell RNA sequencing data, cell populations were annotated using ScType (Fig. 1C). Notably, the abundance of astrocytes differed markedly between the MCAO and control groups. Cell-cell communication analysis revealed differences in both the number and strength of cellular interactions between groups (Fig. 1D). Pseudo-bulk analysis of the single-cell dataset identified 1,031 upregulated genes and 1,108 downregulated genes (Fig. 1E). Finally, Venn diagram analysis identified 27 overlapping hub genes among conventional DEGs, pseudo-bulk DEGs (microglial DEGs), WGCNA-derived genes, and microglia-related marker genes (Fig. 1F). Gene Ontology analysis demonstrated that these hub genes were primarily enriched in leukocyte migration within the biological process category, plasma membrane raft within the cellular component category, and chemokine activity within the molecular function category (Fig. 1G).

Target genes and their corresponding TFs were identified by PPI, machine learning, and FIMO analyses. The protein products encoded by the 27 hub genes and their interactions were analysed using a PPI network with a combined interaction score >0.4 (Fig. 2A). The top 10 hub nodes identified within the PPI network are also presented in Fig. 2A. To further identify key genes, LASSO regression analysis was performed. The coefficient path plot and binomial deviance curves used to evaluate model performance are shown in the left and right panels of Fig. 2B, respectively. This analysis identified four candidate hub genes.

RF analysis was subsequently performed, and five candidate genes were selected from the top 10 hub genes based on the mean decrease in Gini coefficient (Fig. 2C). Among these genes, CCL9 exhibited the highest mean decrease in Gini coefficient. The overlap between the LASSO and RF algorithms identified two common candidate genes, CCL9 and CSF1R (Fig. 2D). The expression levels of both genes were validated in bulk RNA-sequencing and single-cell RNA-sequencing datasets (Fig. 2E and F; $P<0.0001$ for both).

Potential TFs regulating CCL9 and CSF1R were predicted using the TRRUST and JASPAR databases. A total of 27 TFs and 13 TFs were identified from the JASPAR and TRRUST databases, respectively. Three TFs, SPI1, ETS1 and RUNX1, were common to both prediction datasets (Fig. 2G). All three TFs were significantly upregulated in the bulk RNA-sequencing dataset (Fig. 2H). Their predicted regulatory relationships with the target genes are illustrated in Fig. 2I ($P<0.0001$ for all comparisons).

OGD/R microglial is regulated via a ROS- SPI1-CCL9 axis. Compared with the si-NC group, intracellular ROS levels were significantly increased following OGD/R treatment ($P=0.0006$). OGD/R also promoted ROS accumulation in microglia transfected with SPI1 siRNA ($P=0.0034$). However, no significant differences in ROS levels were observed between the si-NC and SPI1 siRNA groups under either normoxic or OGD/R conditions ($P=0.8452$ and 0.8503, respectively; Fig. 3A).

Furthermore, OGD/R significantly increased the mRNA expression of SPI1 and CCL9, whereas SPI1 knockdown significantly attenuated the expression of both (Fig. 3B; $P=1.8374\times10^{-13}$ and 1.3556×10^{-13}, respectively). Consistent with the mRNA results, SPI1 siRNA significantly reduced the protein expression levels of SPI1 and CCL9 ($P=0.0350$ and 0.0001, respectively). OGD/R treatment significantly increased SPI1 and CCL9 protein expression compared with the si-NC group ($P=7.1004\times10^{-8}$ and 2.8229×10^{-9}, respectively), whereas SPI1 knockdown effectively suppressed these increases ($P=1.9895\times10^{-7}$ and 2.5886×10^{-9}, respectively) (Fig. 3C).

ChIP-qPCR analysis was performed to assess SPI1 binding to the CCL9 promoter (Fig. 3D). OGD/R-treated microglia transfected with si-NC exhibited significantly higher enrichment of the CCL9 promoter than the SPI1 knockdown group ($P=3.3648\times10^{-5}$). In addition, SPI1 occupancy at the CCL9 promoter was significantly reduced following SPI1 knockdown compared with the si-NC and OGD/R-treated si-NC groups ($P=0.0196$ and 0.0016, respectively), indicating that SPI1 directly regulates CCL9 transcription.

OGD/R promotes macrophage polarisation towards the M1 phenotype and enhances macrophage migration towards microglia. As shown by the Transwell assay in Fig. 4A, fewer macrophages migrated to the lower chamber in the SPI1 siRNA group than in the si-NC group; however, the difference was not statistically significant ($P=0.4908$). OGD/R-treated

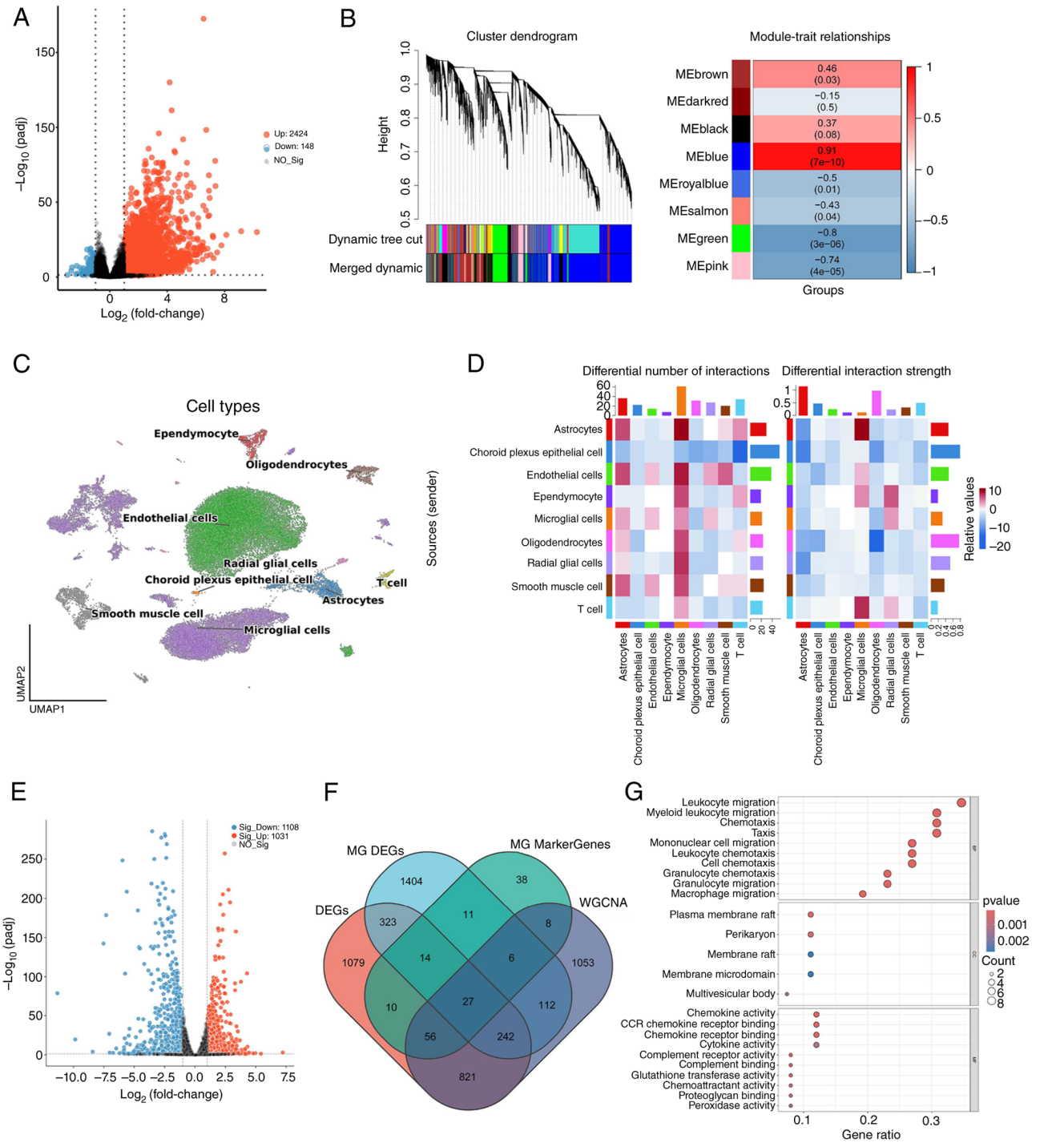


Figure 1. Hub genes were screened from public datasets. (A) Volcano plot of transcriptomics data from GSE137482. (B) WGCNA phenotypes of control and MCAO groups and related gene modules to MCAO. The left chart shows a hierarchical clustering dendrogram. The right chart shows a heatmap of the eight modules for the trait/MCAO relationship. (C) Cellular annotation from single-cell RNA sequencing. (D) Cell-cell interactions from single-cell RNA sequencing. (E) Pseudo-bulk analysis for the single-cell RNA sequencing dataset. The volcano plot shows upregulated and downregulated pseudo-bulk genes. (F) Venn diagram showing the intersection of DEGs, MG DEGs, MG Marker Genes and WGCNA, including 27 hub genes. (G) GO analysis of 27 hub genes. WGCNA, weighted gene co-expression network analysis; MCAO, middle cerebral artery occlusion; DEG, differentially expressed gene; MG, microglia; GO, Gene Ontology.

microglia significantly increased macrophage migration compared with the control group (P=0.0005). Notably, SPI1 knockdown significantly reduced macrophage migration induced by OGD/R treatment (P=0.0045).

Macrophage M1 polarisation was evaluated by measuring the mRNA expression of iNOS, IL-1β and TNF-α using RT-qPCR (Fig. 4B). No significant differences in the expression of these markers were observed between the si-NC and SPI1 siRNA groups under basal conditions [P=0.1393 (iNOS), 0.1174 (IL-1β) and 0.3511 (TNF-α)]. By contrast, OGD/R treatment significantly increased the expression of iNOS, IL-1β, and TNF-α compared with the SPI1 siRNA group

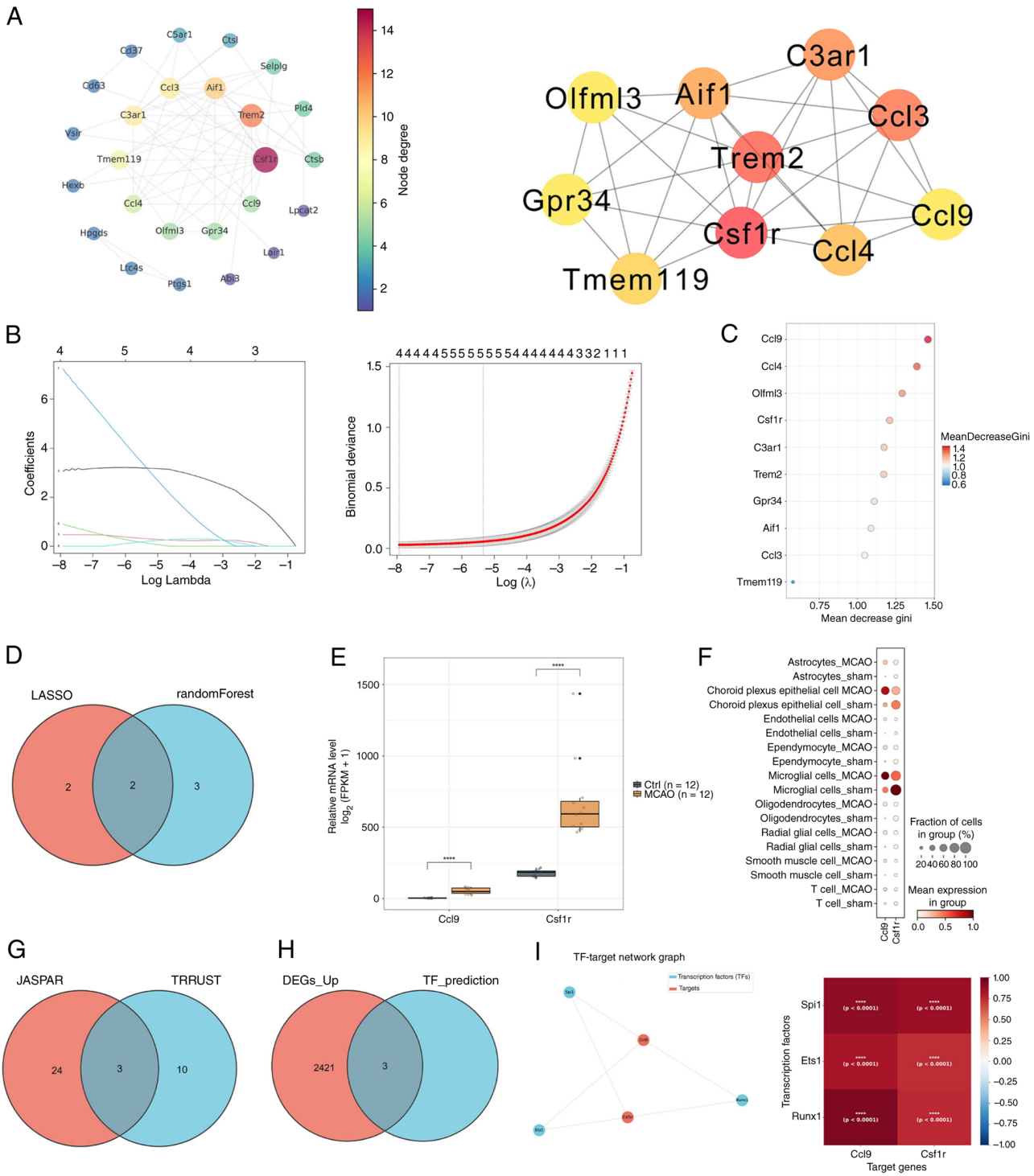


Figure 2. Target genes were screened with PPI, ML and FIMO. (A) PPI of hub genes and top 10 nodes in the network. (B) The coefficient path plot (left) and the binomial deviance plot (right) show the filtering approach using LASSO regression. (C) The plot shows the mean decrease in the Gini coefficient achieved by the Random Forest algorithm for the top 10 related proteins. CCL9 possessed the lowest mean decrease in Gini. (D) Venn diagram of two ML algorithms. The overlapping areas include two genes: CCL9 and CSF1R. (E) CCL9 and CSF1R expression levels were confirmed in a bulk RNA sequencing dataset. (F) CCL9 and CSF1R expression levels were identified in a single-cell RNA sequencing dataset. (G) Venn diagram shows the intersection of TFs predicted with the TRRUST and JASPAR databases. (H) Venn diagram showing the upregulated TFs in the overlap between upregulated DEGs and predicted TFs. (I) Network of TFs and their regulated genes. PPI, protein-protein interaction; ML, machine learning; FIMO, Find Individual Motif Occurrences; LASSO, least absolute shrinkage and selection operator; TF, transcription factor; TRRUST, transcriptional regulatory relationships unravelled by sentence-based text mining; JASPAR, Joint Academic Research Project database; DEG, differentially expressed gene.

(P=0.0002, 1.1588x10^{-11} and 6.6866x10^{-9}, respectively). These OGD/R-induced increases were significantly attenuated by SPI1 knockdown [P=0.0062 (iNOS), 7.7248x10^{-8} (IL-1β) and 1.2270x10^{-7} (TNF-α)].

Flow cytometric analysis demonstrated that the proportion of CD68-positive M1 macrophages increased from 8.2±0.2% in the control group to 18.1±0.3% following OGD/R treatment (P=0.0005; Fig. 4C). This increase was

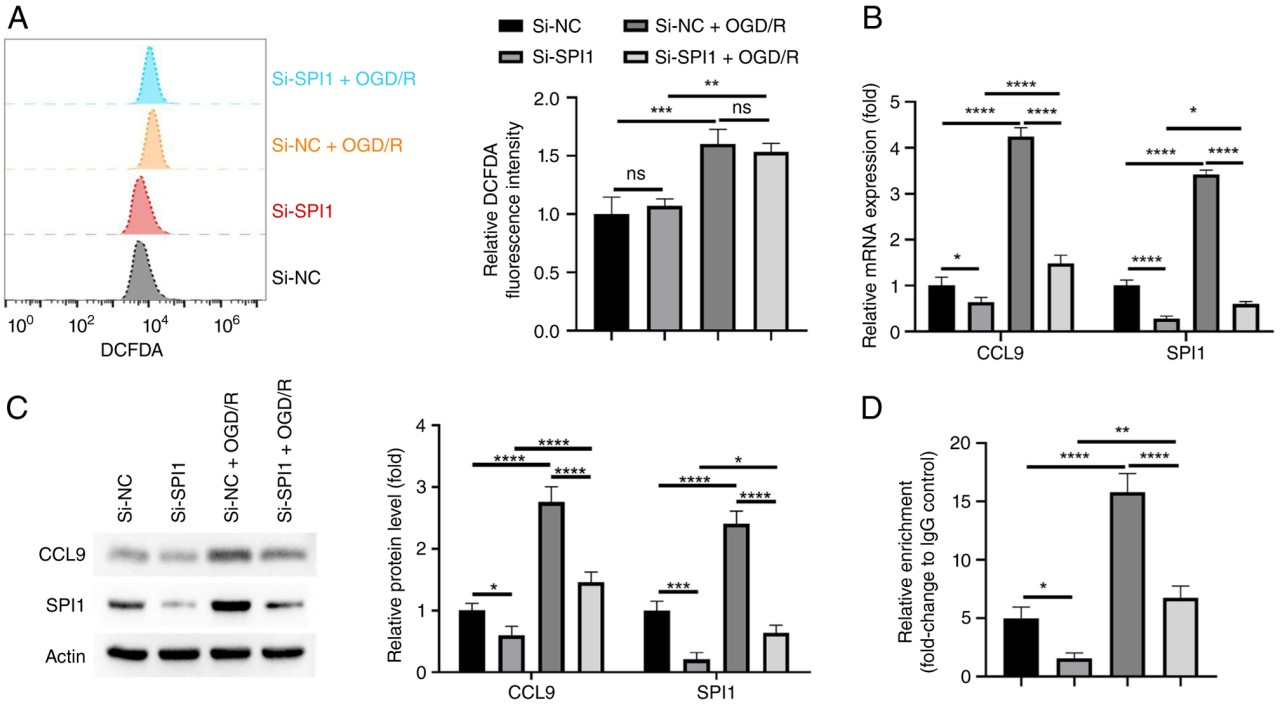


Figure 3. ROS-SPI1-CCL9 axis plays an important role *in vitro*. (A) ROS measurement with flow cytometry. (B) Reverse transcription-quantitative PCR was used to measure CCL9 and SPI1 RNA levels. (C) Western blotting was used to examine relative protein levels of CCL9 and SPI1. (D) Chromatin immunoprecipitation-quantitative PCR tested SPI1 binding to the CCL9 promoter. Data are expressed as the mean ± SD of five independent repeats. Significant differences between groups were identified using a Student's t-test or Mann-Whitney U test. *P<0.05, **P<0.01, ***P<0.001 and ****P<0.0001. ROS, reactive oxygen species; si-, small interfering; NC, negative control; ns, not significant.

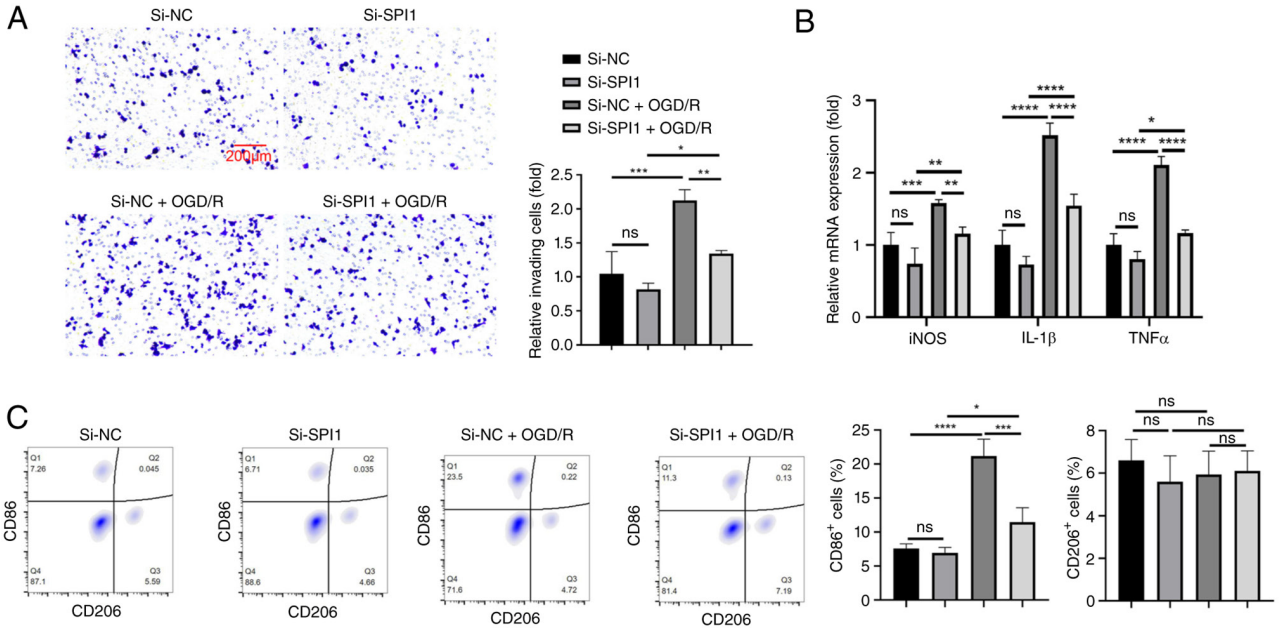


Figure 4. Macrophage polarization and invasion after microglial cells were treated with oxygen-glucose deprivation/reperfusion. (A) Transwell assay for macrophage migration. (B) Macrophages polarized into the M1 type. (C) M1-type-related positive and negative biomarkers were measured with flow cytometry. Data are expressed as the mean ± SD of five independent repeats. Significant differences between groups were identified using a Student's t-test or Mann-Whitney U test. *P<0.05, **P<0.01, ***P<0.001 and ****P<0.0001. ROS, reactive oxygen species; si-, small interfering; NC, negative control; ns, not significant; iNOS, inducible nitric oxide synthase.

significantly reduced to 11.3±0.4% following SPI1 knockdown. By contrast, the proportion of CD206-positive M2 macrophages did not differ significantly among the SPI1 siRNA, OGD/R-treated, and OGD/R plus SPI1 siRNA groups (P=0.9968 and 0.9299, respectively). These results indicate that OGD/R promotes macrophage polarisation towards the M1 phenotype, whereas SPI1 knockdown suppresses this pro-inflammatory response.

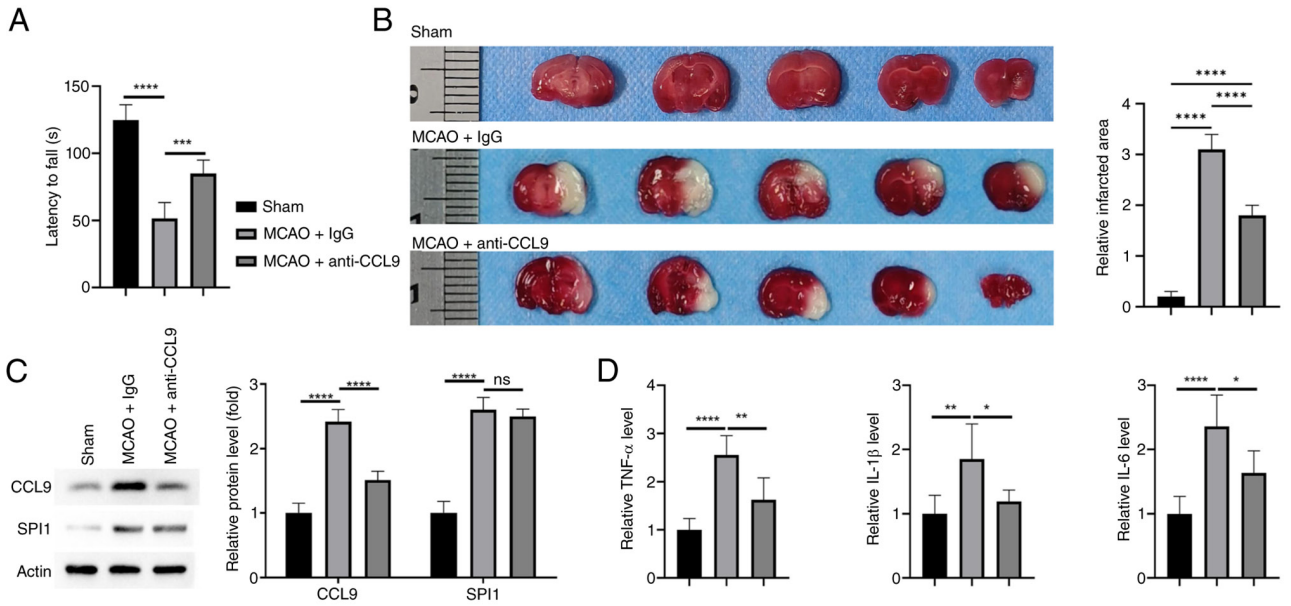


Figure 5. *In vivo* study of MCAO and ischemic injury. (A) Rotarod test in mice from three groups: Sham, MCAO + IgG and MCAO + anti-CCL9 antibody. (B) 2,3,5-triphenyltetrazolium chloride staining shows normal brain tissue with deep red and ischemic tissue with pale or white areas on the left; the right bar chart shows significant differences among groups. (C) Western blotting was used to measure CCL9 and SPI1 levels in ischemic brain tissues. (D) Proinflammatory cytokines were measured using ELISA. Data are expressed as the mean ± SD of five independent repeats. Significant differences between groups were identified using a Student's t-test or Mann-Whitney U test. *P<0.05, **P<0.01, ***P<0.001 and ****P<0.0001. ROS, reactive oxygen species; MCAO, middle cerebral artery occlusion; ns, not significant.

Anti-CCL9 treatment alleviates the effects of MCAO in mice. In the rotarod test evaluating locomotor function, mice in the MCAO + IgG group exhibited a significantly shorter latency to fall (42.3±10.8 sec) than mice in the sham group (125.4±15.6 sec; P=2.5536x10^{-8}), indicating substantial motor impairment following MCAO (Fig. 5A). By contrast, treatment with the anti-CCL9 antibody significantly improved motor performance, increasing the latency to fall to 89.7±12.5 sec compared with the MCAO + IgG group (P=0.0003). These findings suggest that CCL9 blockade alleviates MCAO-induced deficits in balance, coordination and motor endurance.

TTC staining revealed marked differences in cerebral infarction among the experimental groups (Fig. 5B). Brain sections from sham-operated mice showed uniform deep-red staining, indicating viable, metabolically active tissue. By contrast, MCAO mice exhibited prominent pale or white regions, particularly within the cortex and striatum, corresponding to infarcted tissue. Quantitative analysis showed infarct volume of 0.2±0.1% in the sham group, 3.1±0.3% in the MCAO + IgG group, and 1.8±0.2% in the anti-CCL9-treated group. The infarct area was significantly reduced following anti-CCL9 treatment compared with the MCAO + IgG group (P=4.4640x10^{-7}), indicating a neuroprotective effect of CCL9 inhibition.

Western blot analysis demonstrated significant alterations in CCL9 and SPI1 protein expression in brain tissue following MCAO (Fig. 5C). Compared with the sham group, MCAO significantly increased CCL9 expression (P=4.7539x10^{-7}). Anti-CCL9 treatment significantly reduced CCL9 protein levels compared with the MCAO + IgG group (P=4.9048x10^{-5}). By contrast, SPI1 expression was significantly elevated in both the MCAO + IgG and MCAO + anti-CCL9 groups relative to the sham group (P=1.2020x10^{-7} and 2.4986x10^{-7}, respectively). No significant difference in SPI1 expression was observed between the MCAO + IgG and MCAO + anti-CCL9 groups (P=0.7261).

As shown in Fig. 5D, ELISA analysis demonstrated significant changes in the levels of the pro-inflammatory cytokines IL-1β, IL-6 and TNF-α. The TNF-α level in the MCAO + anti-CCL9 group was significantly higher than in the sham group (P=0.0283) but significantly lower than in the MCAO + IgG group (P=0.0018). Similar expression patterns were observed for IL-1β and IL-6. These results indicate that anti-CCL9 treatment attenuated the inflammatory response induced by MCAO, although cytokine levels did not fully return to the baseline values observed in sham-operated mice.

Discussion

In the present study, an *in vitro* cerebral I/R model was established in microglia using the OGD/R approach, while an *in vivo* cerebral I/R model was established in mice using MCAO. The target gene CCL9 was identified through bioinformatics analyses, including machine-learning algorithms, PPI network analysis, TF prediction and related approaches. It was hypothesised that activation of the ROS-SPI1-CCL9 axis in microglia would induce increased CCL9 expression, thereby enhancing macrophage infiltration into cerebral tissue and promoting M1 polarisation, resulting in elevated IL-1β, IL-6 and TNF-α levels that contribute to disease pathogenesis. The present study suggested that suppression of SPI1 and CCL9 may represent a novel therapeutic strategy for mitigating cerebral I/R injury.

Cerebral I/R injury is a complex pathological process characterised by the initial interruption of blood flow followed by its restoration, which paradoxically exacerbates tissue damage.

Microglia and macrophages, as the primary immune cells of the central nervous system (CNS), play pivotal roles in the progression of I/R injury. Microglia are the first responders to ischaemic insult, rapidly transitioning from a surveillant state to an activated phenotype. This activation is characterised by morphological changes, including the extension of cellular processes towards the injury site, and functional alterations, such as the release of pro-inflammatory cytokines including TNF-α, IL-1β and IL-6, which contribute to neuronal damage (8,12). However, microglia also exhibit diverse functions. Single-cell RNA sequencing has identified eight distinct microglial subpopulations during the acute phase of ischaemic stroke, including homeostatic, pre-activated, and low-inflammatory clusters, each with unique gene expression profiles and functional characteristics (10,12,23,24). The present study demonstrated that microglia expressed increased levels of CCL9 under the regulation of Spi1 following OGD/R exposure, which was used to simulate cerebral I/R injury. Under conditions of oxidative stress, microglia predominantly remained in an activated state, as evidenced by the increased expression of CCL9, IL-1β and IL-6 (25). The interaction between microglia and macrophages is a critical component of cerebral I/R injury. Following disruption of the BBB, peripheral monocytes infiltrate the ischaemic brain and differentiate into macrophages. These cells exhibit phenotypic plasticity and can polarise into either pro-inflammatory (M1) or anti-inflammatory (M2) macrophages, depending on the local microenvironment (26). The findings suggested that CCL9-expressing microglia promote M1 macrophage polarisation rather than M2 polarisation, leading to increased secretion of pro-inflammatory cytokines, including IL-1β, IL-6 and TNF-α, in the cerebral I/R microenvironment.

The TF Spi1 (PU.1) plays a critical role in regulating myeloid-cell development and function (27). In the context of fibrosis, SPI1 has been identified as a key regulator of fibroblast activation, a process often associated with the production of extracellular matrix components and inflammatory mediators (28). Zong *et al* (29) reported that Spi1 binds to the Gata2 promoter and enhances its transcription, thereby promoting early activation of interstitial fibroblasts during I/R-induced acute kidney injury. The role of Spi1 also extends to neuroinflammation and microglial maintenance. Spi1 is essential for microglial survival and function, and conditional deletion of Spi1 results in microglial depletion via apoptosis, highlighting its dosage-dependent role in microglial homeostasis (30). Furthermore, SPI1 contributes to the transcriptional regulation of pro-inflammatory genes in microglia and has therefore been proposed as a target for RNA-based therapeutics to reduce neuroinflammation in neurodegenerative diseases (31). Xu *et al* (32) used luciferase assays and ChIP-PCR analyses to demonstrate that Spi1 binds directly to the Clec7a promoter. Both *in vivo* and *in vitro* rescue experiments further showed that Spi1 exacerbates pain sensitivity, promotes neuroinflammation, and enhances microglial phagocytosis through its interaction with Clec7a.

CCL9 has been shown to directly activate hepatic stellate cells in models of liver fibrosis through a mechanism involving recruitment of Myh9 via the CCR1 receptor. This interaction enhances Wnt signalling, thereby promoting fibrosis and tissue damage (33). Treatment of microglia with glioma-conditioned medium rapidly increased the expression of several CCR1 ligands, including CCL9, CCL3, CCL5 and CCL6 (34). These findings suggest the existence of a tumour-induced autocrine loop in tumour-associated macrophages and microglia that facilitates tumour-cell invasion. Furthermore, the role of CCL9 is not restricted to cancer. Baba *et al* (35) reported sustained expression of CCL9, CCL5 and CXCL1 from the post-injury period through day 21 following neonatal mouse brain I/R injury. These observations suggest that CCL9 may modulate microglial phagocytic activity, cytokine production, and migratory behaviour, thereby contributing to the progression of neuroinflammatory and neurodegenerative processes.

The functional significance of CCL9 in microglia may be inferred from its structural and signalling similarities to other chemokines. Chemokines typically bind to G-protein-coupled receptors on microglia, triggering intracellular signalling cascades that regulate cellular functions (36). If CCL9 follows this paradigm, it could activate pathways such as PI3K/Akt or MAPK, which are known to influence microglial activation and inflammatory responses (37). Furthermore, the interplay between CCL9 and other chemokines or receptors, such as CCR1 or CCR5, could determine its specific contributions to microglial dynamics. Innovatively, targeting CCL9 signalling in microglia could offer therapeutic potential for neuroinflammatory and neurodegenerative diseases. By modulating CCL9 expression or its receptor interactions, it may be possible to fine-tune microglial activation, reducing detrimental pro-inflammatory responses while preserving their beneficial roles in tissue repair and homeostasis.

Several limitations of the present study deserve discussion. First, the hub genes were mined and screened from transcriptomic and single-cell RNA sequencing datasets in public databases. The sample sizes of these datasets may be limited, which may affect the robustness and generalizability of the identified hub genes. Additionally, computational techniques were used to filter key hub genes and identify the ROS-SPI1-CCL9 axis, and *in vivo* experiments were performed to validate the *in vitro* model and mechanism. However, the findings might not be translated into conditions of human ischemic stroke owing to species disparity. Although ChIP-qPCR confirmed that SPI1 bound to the CCL9 promoter, other TFs or epigenetic modifications that could also regulate CCL9 expression were not investigated. Finally, this exploratory research, with a small sample size, lacked a human biopsy to corroborate our hypothesis and findings and instead relied on a confirmatory assessment.

In conclusion, while direct evidence that Spi1 regulates CCL9 in microglia to promote macrophage infiltration and polarization CCL9 is limited, its potential roles in cerebral I/R in cerebral ischemic stroke remain. By leveraging insights from related chemokine pathways and microglial biology, future studies could elucidate the mechanisms and therapeutic potential of CCL9 in neuroinflammatory and neurodegenerative diseases. This research could pave the way for novel interventions targeting microglial chemokine signalling, ultimately improving outcomes for patients with CNS disorders.

Acknowledgements

Not applicable.

Funding

The present study was supported in part by the Kunming Medical University Master's Graduate Innovation Fund (grant no. 2024S056), the Yunnan Revitalization Talent Support Program (grant nos. XDYC-QNRC-2022-0293 and XDYC-Q NRC-2022-0263) and National Natural Science Foundation of China (grant nos. 82560697 and 82260098).

Availability of data and materials

The data generated in the present study may be requested from the corresponding author.

Authors' contributions

All authors were involved in the conceptualization and design of the study. XK was responsible for the core concept of this research, formulated the research framework, and undertook the tasks of designing and implementing the experimental protocol. ZP and YY were responsible for data collection and the analysis of target genes. SP, MZ and JW carried out the statistical evaluation of the experimental findings. JT and SL participated the research conceptualization and confirmed the authenticity of all the raw data. DZ provided oversight and supervision for the entire study and offered critical revisions to the manuscript. All authors read and approved the final version of the manuscript.

Ethics approval and consent to participate

Animal experiments were approved by the Institutional Animal Care and Use Committee of the Kunming Medical University (approval no: KMMU 20240416; Kunming, China).

Patient consent for publication

Not applicable.

Competing interests

The authors declare that they have no competing interests.

References

1. Zhao Y, Zhang X, Chen X and Wei Y: Neuronal injuries in cerebral infarction and ischemic stroke: From mechanisms to treatment (Review). Int J Mol Med 2022, 49: 15, 2022.
2. Wang Q, Yang F, Duo K, Liu Y, Yu J, Wu Q and Cai Z: The role of necroptosis in cerebral ischemic stroke. Mol Neurobiol 61: 3882-3898, 2024.
3. L L, X W and Z Y: Ischemia-reperfusion Injury in the Brain: Mechanisms and potential therapeutic strategies. Biochem Pharmacol (Los Angel) 5: 2013, 2016.
4. She R, Liu D, Liao J, Wang G, Ge J and Mei Z: Mitochondrial dysfunctions induce PANoptosis and ferroptosis in cerebral ischemia/reperfusion injury: From pathology to therapeutic potential. Front Cell Neurosci 17: 1191629, 2023.
5. Gong L, Liang J, Xie L, Zhang Z, Mei Z and Zhang W: Metabolic reprogramming in gliocyte post-cerebral ischemia/reperfusion: From pathophysiology to therapeutic potential. Curr Neuropharmacol 22: 1672-1696, 2024.
6. Hong JM, Kim DS and Kim M: Hemorrhagic transformation after ischemic stroke: Mechanisms and management. Front Neurol 12: 703258, 2021.
7. Wang Y, Wang Y, Li S, Cui Y, Liang X, Shan J, Gu W, Qiu J, Li Y and Wang G: Functionalized nanoparticles with monocyte membranes and rapamycin achieve synergistic chemoimmunotherapy for reperfusion-induced injury in ischemic stroke. J Nanobiotechnology 19: 331, 2021.
8. Ma Y, Li Y, Jiang L, Wang L, Jiang Z, Wang Y, Zhang Z and Yang GY: Macrophage depletion reduced brain injury following middle cerebral artery occlusion in mice. J Neuroinflammation 13: 38, 2016.
9. Kestner RI, Mayser F, Vutukuri R, Hansen L, Günther S, Brunkhorst R, Devraj K and Pfeilschifter W: Gene expression dynamics at the neurovascular unit during early regeneration after cerebral ischemia/reperfusion injury in mice. Front Neurosci 14: 280, 2020.
10. Li T, Zhao J, Xie W, Yuan W, Guo J, Pang S, Gan WB, Gómez-Nicola D and Zhang S: Specific depletion of resident microglia in the early stage of stroke reduces cerebral ischemic damage. J Neuroinflammation 18: 81, 2021.
11. Liu DQ, Mei W, Zhou YQ and Xi H: Targeting TRPM channels for cerebral ischemia-reperfusion injury. Trends Pharmacol Sci 45: 862-867, 2024.
12. Ma H, Li H, Zhang Y, Zhou Y, Liu H, Xu H, Zhu L, Zhang G, Wang J, Li Z, *et al*: Microglia exhibit distinct heterogeneity rather than M1/M2 polarization within the early stage of acute ischemic stroke. Aging Dis 14: 2284-2302, 2023.
13. Androvic P, Kirdajova D, Tureckova J, Zucha D, Rohlova E, Abaffy P, Kriska J, Valny M, Anderova M, Kubista M and Valihrach L: Decoding the transcriptional response to ischemic stroke in young and aged mouse brain. Cell Rep 31: 107777, 2020.
14. Zheng K, Lin L, Jiang W, Chen L, Zhang X, Zhang Q, Ren Y and Hao J: Single-cell RNA-seq reveals the transcriptional landscape in ischemic stroke. J Cereb Blood Flow Metab 42: 56-73, 2022.
15. Hao Y, Stuart T, Kowalski MH, Choudhary S, Hoffman P, Hartman A, Srivastava A, Molla G, Madad S, Fernandez-Granda C and Satija R: Dictionary learning for integrative, multimodal and scalable single-cell analysis. Nat Biotechnol 42: 293-304, 2024.
16. Wolf FA, Angerer P and Theis FJ: SCANPY: Large-scale single-cell gene expression data analysis. Genome Biol 19: 15, 2018.
17. Love MI, Huber W and Anders S: Moderated estimation of fold change and dispersion for RNA-seq data with DESeq2. Genome Biol 15: 550, 2014.
18. Breiman L: Random Forests. Machine Learning 45: 5-32, 2001.
19. Friedman J, Hastie T and Tibshirani R: Regularization paths for generalized linear models via coordinate descent. J Stat Softw 33: 1-22, 2010.
20. Livak KJ and Schmittgen TD: Analysis of relative gene expression data using real-time quantitative PCR and the 2(-Delta Delta C(T)) Method. Methods 25: 402-408, 2001.
21. de Oliveira JL, Ávila M, Martins TC, Alvarez-Silva M, Winkelmann-Duarte EC, Salgado ASI, Cidral-Filho FJ, Reed WR and Martins DF: Medium- and long-term functional behavior evaluations in an experimental focal ischemic stroke mouse model. Cogn Neurodyn 14: 473-481, 2020.
22. Nouraee C, Fisher M, Di Napoli M, Salazar P, Farr TD, Jafarli A and Divani AA: A brief review of edema-adjusted infarct volume measurement techniques for rodent focal cerebral ischemia models with practical recommendations. J Vasc Interv Neurol 10: 38-45, 2019.
23. Yeo HG, Hong JJ, Lee Y, Yi KS, Jeon CY, Park J, Won J, Seo J, Ahn YJ, Kim K, *et al*: Increased CD68/TGFβ co-expressing microglia/macrophages after transient middle cerebral artery occlusion in rhesus monkeys. Exp Neurobiol 28: 458-473, 2019.
24. Zhang C, Brandon NR, Koper K, Tang P, Xu Y and Dou H: Invasion of peripheral immune cells into brain parenchyma after cardiac arrest and resuscitation. Aging Dis 9: 412-425, 2018.
25. Akhtar F, Rouse CA, Catano G, Montalvo M, Ullevig SL, Asmis R, Kharbanda K and Maffi SK: Acute maternal oxidant exposure causes susceptibility of the fetal brain to inflammation and oxidative stress. J Neuroinflammation 14: 195, 2017.
26. Xie X, Liu X, Zhu J, Xu Y, Li X, Zheng Y, Gong S, Xiao X, Chen Y, Zhang J, *et al*: Long-term microglial phase-specific dynamics during single vessel occlusion and recanalization. Commun Biol 5: 841, 2022.
27. Gregoricchio S, Polit L, Esposito M, Berthelet J, Delestré L, Evanno E, Diop M, Gallais I, Aleth H, Poplineau M, *et al*: HDAC1 and PRC2 mediate combinatorial control in SPI1/PU.1-dependent gene repression in murine erythroleukaemia. Nucleic Acids Res 50: 7938-7958, 2022.

28. Wohlfahrt T, Rauber S, Uebe S, Luber M, Soare A, Ekici A, Weber S, Matei AE, Chen CW, Maier C, *et al*: PU.1 controls fibroblast polarization and tissue fibrosis. Nature 566: 344-349, 2019.
29. Zong C, Xu GL, Ning M, Li JY, Wang X, Guo HJ, Zhang LH, Zhou L, Xu C, Yang ZH, *et al*: PU.1/Spi1 exacerbates ischemia-reperfusion induced acute kidney injury via upregulating Gata2 and promoting fibroblast activation. Acta Pharmacol Sin 46: 2251-2266, 2025.
30. Wu Y, Guo W, Kuang H, Wu X, Trinh TH, Wang Y, Zhao S, Wen Z and Yu T: Pu.1/Spi1 dosage controls the turnover and maintenance of microglia in zebrafish and mammals. Elife 14: RP105788, 2025.
31. Ralvenius WT, Andresen JL, Huston MM, Penney J, Bonner JM, Fenton OS, Langer R and Tsai LH: Nanoparticle-mediated delivery of Anti-PU.1 siRNA via localized intracisternal administration reduces neuroinflammation. Adv Mater 36: e2309225, 2024.
32. Xu Y, Liu X, Chen H, Zhao Y, Zhao Y, Xie Y, Pang J, Zeng H, Zeng Y, Peng W, *et al*: Spi1 aggravates neuropathic pain by modulating Clec7a-mediated neuroinflammation and microglial phagocytosis. J Headache Pain 26: 158, 2025.
33. Wang C, Dong D, Zhao N, Zhao S, Hua J, Bai C, Cui R, Zhao T, Ji N, Li H, *et al*: Hepatocyte-specific C-C motif chemokine ligand 9 signaling promotes liver fibrosis progression in mice. Hepatology 83: 789-807, 2026.
34. Zeren N, Afzal Z, Morgan S, Marshall G, Uppiliappan M, Merritt J and Coniglio SJ: The chemokine receptor CCR1 mediates microglia stimulated glioma invasion. Int J Mol Sci 24: 5136, 2023.
35. Baba N, Wang F, Iizuka M, Shen Y, Yamashita T, Takaishi K, Tsuru E, Matsushima S, Miyamura M, Fujieda M, *et al*: Induction of regional chemokine expression in response to human umbilical cord blood cell infusion in the neonatal mouse ischemia-reperfusion brain injury model. PLoS One 14: e0221111, 2019.
36. Dong L, Li YZ, An HT, Wang YL, Chen SH, Qian YJ, Wang K, Zhen JL, Fan Z, Gong XL, *et al*: The E3 ubiquitin ligase c-Cbl inhibits microglia-mediated CNS inflammation by regulating PI3K/Akt/NF-κB pathway. CNS Neurosci Ther 22: 661-669, 2016.
37. Wlodarczyk A, Benmamar-Badel A, Cédile O, Jensen KN, Kramer I, Elsborg NB and Owens T: CSF1R stimulation promotes increased neuroprotection by CD11c+ Microglia in EAE. Front Cell Neurosci 12: 523, 2019.

Copyright © 2026 Kuang et al. This work is licensed under a Creative Commons Attribution-NonCommercial-NoDerivatives 4.0 International (CC BY-NC-ND 4.0) License.